



Cite this: *Nanoscale Adv.*, 2025, 7, 2709

# Development of a crystalline n-AgBr/p-NiO binary heterojunction for photocatalytic degradation of organic contaminants with accompanying mineralization, adsorption, and antimicrobial studies†

Murad Z. A. Warshagha,<sup>‡a</sup> Ziyaur Rasool,<sup>‡a</sup> Mohammad Saud Athar,<sup>a</sup> Mohammad Muneer,<sup>‡a</sup> <sup>‡a</sup> Hatem M. Altass,<sup>b</sup> Raad Felemban,<sup>c</sup> Abdelrahman S. Khder<sup>b</sup> and Saleh A. Ahmed <sup>‡b</sup>

A highly effective and unique AgBr–NiO binary heterojunction was developed using an effective one-pot sol–gel method. The physicochemical properties of the produced materials were carefully examined using analytical techniques, including X-ray diffraction (XRD), scanning electron microscopy (SEM), energy dispersive X-ray (EDX) analysis, transmission electron microscopy (TEM), Brunauer–Emmett–Teller (BET), ultraviolet-visible diffuse reflectance spectroscopy (UV-vis-DRS), Fourier transform infrared spectroscopy (FTIR), and photoluminescence (PL). The mesoporous nature and high surface properties of AgBr–NiO were revealed by the BET analysis. The AgBr–NiO composite showed greater photocatalytic degradation efficiency than bare AgBr and NiO when exposed to visible light for the colored anionic dye rhodamine B (RhB) and bisphenol A (BPA), a colorless endocrine-disrupting contaminant (EDC), resulting in high photocatalytic activity for the degradation of RhB (97.6% in 11 min) and BPA (85% in 120 min). Additionally, a notable decrease in TOC over time was observed under similar reaction conditions in the photo-mineralization examination of both model pollutants. Trapping tests were conducted to determine which reactive oxygen species (ROS) were involved in the degradation process. A plausible Z-scheme mechanism for this n–p heterojunction was proposed to explain the formation of  $e^-/h^+$  pairs induced by visible light. The proposed work facilitates the development of a recyclable photocatalyst characterized by high biological activity and low toxicity.

Received 24th December 2024  
Accepted 7th March 2025

DOI: 10.1039/d4na01065e

rsc.li/nanoscale-advances

## 1. Introduction

The rapid growth of industries has made water purification one of the major environmental crises worldwide. Refractory pollutants, such as industrial dyes, heavy metal ions, and antibiotics, pose significant hazards to human health and life.<sup>1–6</sup>

The most serious risks to humans and aquatic life are caused by synthetic dyes, such as RhB, which are used in the leather, cosmetic, and textile industries, as well as other priority

contaminants, such as BPA. These dyes pollute water supplies by being released in large amounts into aquatic ecosystems.<sup>7–13</sup>

As a result, eliminating these organic pollutants requires the use of sustainable and highly efficient methods that can break down complex organic compounds and reduce secondary pollution.<sup>14–17</sup> Among the various approaches to these problems, semiconductor-based photocatalytic methods are considered efficient and sustainable.<sup>18</sup> Photocatalytic technology significantly contributes to environmental protection<sup>19,20</sup> and is considered a preferred method and green approach for air purification and water treatment due to its utilization of solar energy, low cost, and potential for mineralization of organic contaminants.<sup>21–23</sup> Conventional semiconductors, such as TiO<sub>2</sub> and ZnO, being affordable and non-toxic photocatalysts, demonstrate significant photocatalytic activities; however, their wide band gap (2.9–3.2 eV) restricts their ability to absorb visible light and limits their practical applications.<sup>24–27</sup> Moreover, due to the rapid recombination rate of photogenerated electron–hole pairs, these photocatalysts perform moderately.<sup>28,29</sup> Therefore, photochemists are developing

<sup>a</sup>Department of Chemistry, Aligarh Muslim University, Aligarh, 202002, India. E-mail: m.muneer.ch@amu.ac.in

<sup>b</sup>Department of Chemistry, Faculty of Science, Umm Al-Qura University, 21955 Makkah, Saudi Arabia. E-mail: saahmed@uqu.edu.sa

<sup>c</sup>Research Laboratories Unit, Faculty of Science, Umm Al-Qura University, Makkah, Saudi Arabia

† Electronic supplementary information (ESI) available. See DOI: <https://doi.org/10.1039/d4na01065e>

‡ Both authors made equal contributions to this work.

photocatalysts with a narrower band gap that can achieve higher responsiveness to visible light and separate electron-hole pairs more effectively.<sup>30,31</sup>

In the context of highly efficient photocatalysis, silver halides (AgX, where X = I, Br, or Cl) have garnered substantial attention due to their exceptional photosensitivity, which allows them to effectively combine with other semiconductors to enhance light absorption in the visible range and improve their photocatalytic activity.<sup>18,20,32</sup> Among the AgX semiconductors, AgBr, an n-type semiconductor, has garnered much attention due to its narrow band gap, distinctive layered structure, and its ability to activate in the visible light range, all of which contribute to improved photocatalytic activity.<sup>20,32</sup> However, despite these advantages, the photocatalytic performance of pure AgBr is significantly hindered by the rapid recombination of charge carriers and its limited surface area.<sup>33</sup>

To overcome these challenges, a variety of heterojunctions have been fabricated to enhance photocatalytic activity, expand the surface area, and accelerate the separation of photo-generated carriers.<sup>18,20,32–34</sup> AgBr is typically combined with either p-type or n-type semiconductors, leading to various successful heterojunctions, such as AgBr/ $\beta$ -MnO<sub>2</sub>,<sup>20</sup> TiO<sub>2</sub>/Ag<sub>2</sub>WO<sub>4</sub>/AgBr,<sup>33</sup> Ag/AgBr@G,<sup>34</sup> Bi<sub>2</sub>SiO<sub>5</sub>/Ag/AgBr,<sup>35</sup> TiO<sub>2-x</sub>/BiOBr/AgBr,<sup>36</sup> and COF TzDa/Ag/AgBr.<sup>2</sup> However, there have been only a limited number of studies focusing on n-p type heterojunctions of silver halides.

Currently, NiO is recognized as a p-type semiconductor with extensive applications in catalysis, solar cells, and gas sensors.<sup>37</sup> The widespread use of Ni nanoparticles is due to their superior physical and chemical properties.<sup>24,37,38</sup> To date, numerous works have reported on NiO heterojunctions, including p-BiOI/p-NiO,<sup>37</sup> NiO/TiO<sub>2</sub>,<sup>39</sup> NiO/ZnO,<sup>40</sup> NiO/CdS,<sup>41</sup> and NiO/g-C<sub>3</sub>N<sub>4</sub>.<sup>42</sup> Besides, pristine NiO does not exhibit efficient photoactivity. However, pristine AgBr, a prominent absorber of visible light, can sensitize NiO effectively, whereby the fast recombination of photoinduced charge carriers can be inhibited by combining AgBr with NiO. Furthermore, metal oxide-based photocatalysts are known to have antibacterial properties due to their ability to generate ROS. Warshagha *et al.* synthesized a heterojunction photocatalyst containing AgI by a co-participation method and then used this for the degradation of organic compounds, as well as against *E. coli*, *S. aureus*, and *P. aeruginosa*.<sup>20</sup> In addition, Laokul *et al.* examined the activity of the photocatalyst ZnO/ZnS/AgBr for the degradation of methylene blue and methyl orange and the inhibition of Gram-positive as well as Gram-negative bacteria.<sup>43</sup> To achieve these promising outcomes, a precipitation approach was chosen to produce a novel n-AgBr-p-NiO photocatalyst. To date, no reports have been published regarding the synthesis and characterization of n-AgBr/p-NiO nano photocatalysts and their photocatalytic activity compared with bare AgBr and NiO.

In this article, we reported a novel n-AgBr/p-NiO heterojunction fabricated *via* a simple co-participation approach. Its photocatalytic efficiency was examined for the degradation of RhB and BPA in aqueous suspension under visible light irradiation. Additionally, we proposed a photocatalytic scheme that takes into account the respective band positions of the

semiconductors. The characteristic properties of the synthesized materials were examined by XRD, SEM, TEM, EDX mapping, XPS, BET, FTIR, and DRS. Lastly, the antimicrobial efficacy of the synthesized samples was validated by testing them against *Staphylococcus aureus* (*S. aureus*) and *Micrococcus luteus* (*M. luteus*).

## 2. Experimental

### 2.1. Chemicals required, synthesis of the samples, materials characterization, trapping experiments, evaluation of the photocatalytic activity, adsorption and antibacterial studies

Full details of all these aspects are contained in the ESI file.†

## 3. Results and discussion

### 3.1. XRD analysis

The phase purity and crystallinity of the as-produced NiO, AgBr, and xAgBr-NiO ( $x = 0.05, 0.1$ , and  $0.15$  M) were initially examined by powder X-ray diffraction, with the obtained XRD patterns displayed in Fig. 1. The XRD peaks of the nickel oxide sample ( $2\theta = 37.2^\circ, 43.3^\circ, 62.9^\circ, 75.4^\circ$ , and  $79.4^\circ$ ) corresponded to the (111), (200), (220), (311), and (222) cubic crystal structure of NiO, consistent with the standard JCPDS (no. 73-1523).<sup>44</sup> The cubic crystal phase of AgBr was indicated by its various diffraction peaks located at  $2\theta = 26.8^\circ, 31.0^\circ, 44.4^\circ, 55.1^\circ, 64.6^\circ$ , and  $73.3^\circ$  assigned to the (111), (200), (220), (222), (400) and (420) planes, consistent with JCPDS (no. 06-0438).<sup>45</sup> Both the diffraction peaks of the pure samples AgBr and NiO could be clearly detected by the nanostructured photocatalyst. Upon further observation, it was observed that as the weight percentage of the pure AgBr sample increased in the composite, the intensity of the peaks corresponding to NiO diminished significantly. In contrast, the peak intensity of AgBr exhibited

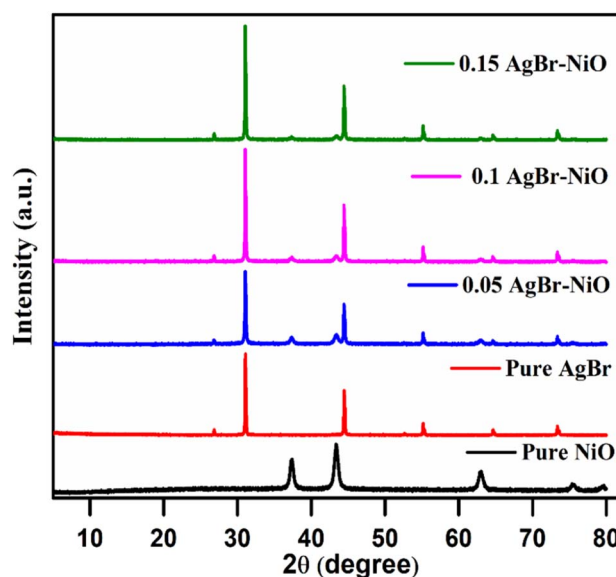


Fig. 1 XRD patterns of bare AgBr, bare NiO, and the xAgBr-NiO n-p heterojunctions.



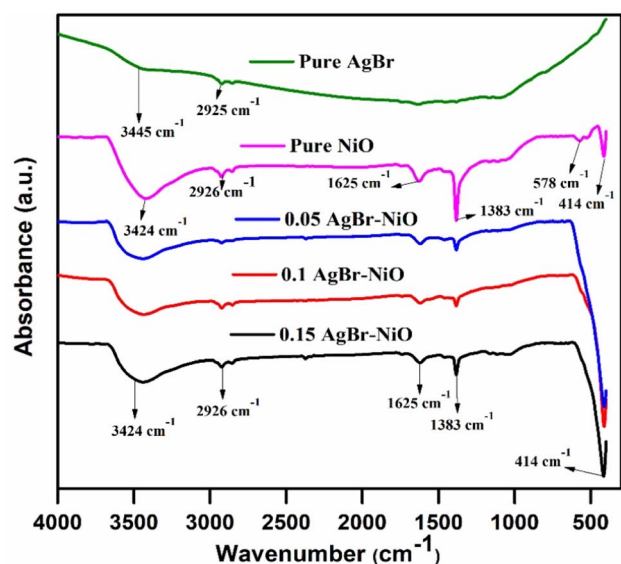


Fig. 2 FTIR spectra of pure AgBr, pure NiO, and the xAgBr–NiO heterojunctions.

a monotonic increase. The absence of any impurity peak in the n-AgBr/p-NiO heterojunctions suggested that AgBr and NiO were the main components of the xAgBr–NiO photocatalysts.

### 3.2. FTIR analysis

An understanding of the functional groups in synthesized samples can be achieved through the use of FTIR spectroscopy. The FTIR spectra of AgBr, NiO, and xAgBr–NiO with different molar ratios are presented in Fig. 2. As shown in Fig. 2, absorption peaks were observed at 414 and 578  $\text{cm}^{-1}$  associated with the vibrational modes of Ni–O bonds. Also, strong peaks were observed for absorption at 1625 and 1383  $\text{cm}^{-1}$ , attributed to the vibrations of the O–H bond and stretching mode of Ni–O–H.<sup>46,47</sup> The broad vibrational bands located at 2926 and 3424  $\text{cm}^{-1}$  corresponded to asymmetric O–H stretching. Absorption bands at 2925 and 3445  $\text{cm}^{-1}$  were observed for AgBr, believed to be caused by the stretching vibration of free

O–H absorbed from  $\text{H}_2\text{O}$ . All the n-AgBr/p-NiO heterojunctions exhibited similar characteristic peaks to both pure samples, *i.e.*, AgBr and NiO, demonstrating the combination of their spectra, and indicating the formation of a covalent bond between them.

### 3.3. SEM analysis

The surface morphologies of the prepared singular NiO and AgBr, and the representative 0.15 AgBr–NiO were characterized by SEM analysis and the results are presented in Fig. 3. The pristine NiO nanoparticles were spherical and nanocluster shaped with a few of them agglomerated, which may have been due to the large heat of the calcination process, as shown in Fig. 3a. Meanwhile, the bare AgBr showed smooth spongy spherical particles that were tightly stacked onto each other, as displayed in Fig. 3b. For the n-AgBr/p-NiO samples, the AgBr spherical nanoparticles were homogeneously scattered across the surface of NiO, exhibiting a slight interlocking without significant agglomeration, as depicted in Fig. 3c. These results confirmed that both phases of pure AgBr and NiO overlapped with each other in the heterojunction sample, which was favorable for modifying the surface of the catalyst.

### 3.4. EDX analysis

To determine the composition of the as-synthesized photocatalysts, EDX analysis of AgBr, NiO, and 0.15 AgBr–NiO was performed. The presence of Ag, Br, O, and Ni could be detected in the EDX spectra of the pure AgBr and NiO, as evident from Fig. 4a and b. In Fig. 4c, it is evident that the n–p heterojunction (0.15 AgBr–NiO) predominantly comprised Ni, O, Ag, and Br elements, and these elements were the main cause of the observed peaks. No additional elemental peaks were found except for the desired elements, and the elements were in a satisfactory stoichiometry. The results thus indicate that the synthetic samples were extremely pure.

### 3.5. HRTEM analysis

The nanostructures of the pure NiO and AgBr, and 0.15 AgBr–NiO composite were further analyzed by HRTEM, as displayed

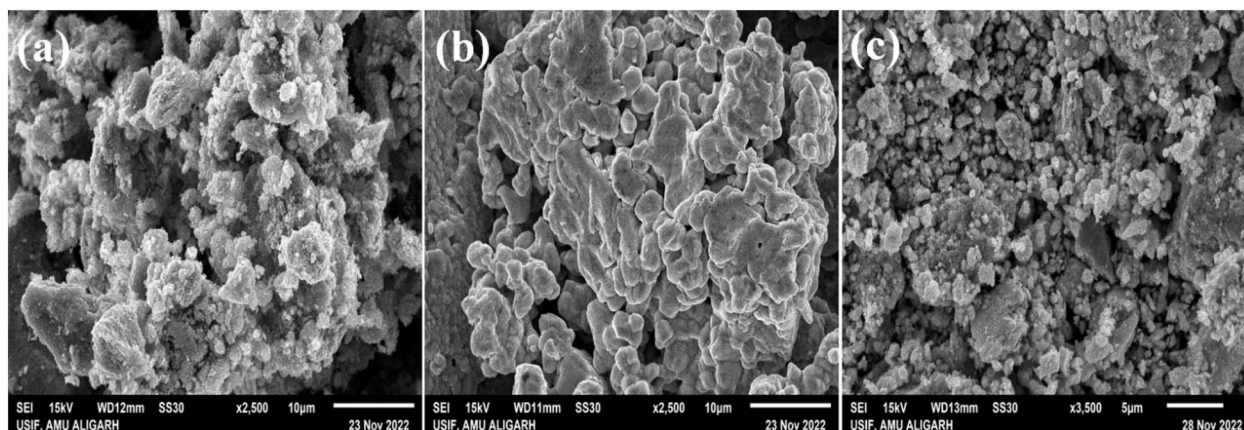
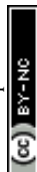


Fig. 3 SEM images of pure NiO (a), pure AgBr (b), and the n–p heterojunction 0.15 AgBr–NiO (c).





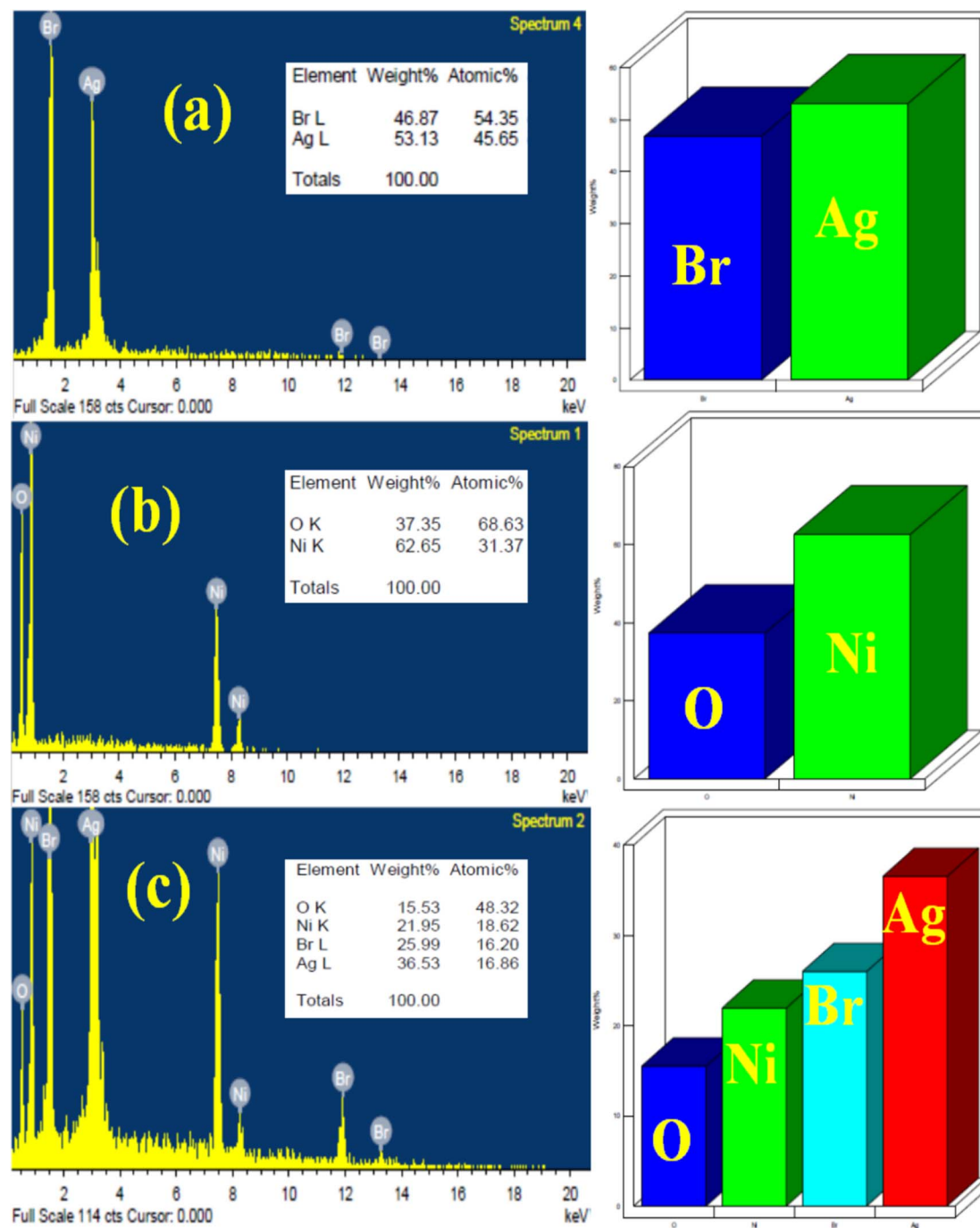


Fig. 4 EDX analysis of bare AgBr (a), bare NiO (b), and the n-p heterojunction 0.15 AgBr-NiO (c).

in Fig. 5. Fig. 5a shows an HRTEM image of the as-prepared NiO NPs, which were spherical with diameters of 20–30 nm. The inset of Fig. 5a shows a high-resolution view of the NiO NPs, which was consistent with the SEM findings. The HRTEM images in Fig. 5b show the interplanar distances of 0.21 nm, and 0.24 nm, corresponding to the (200) and (111) planes of NiO. Fig. 5c shows that the NiO structure consisted of highly crystalline nanocrystals, with the rings assigned to the (111), (200), (220), (311), and (222) planes of NiO, which was in good agreement with the XRD study results. The shape of the AgBr

nanoparticles was spherical, as shown in Fig. 5d. The lattice spacings of 0.235, 0.288, and 0.347 nm corresponded to the (111), (200), and (400) planes of AgBr, in agreement with the XRD data. The SAED pattern in Fig. 5f demonstrated the AgBr nanoparticles were crystalline in nature.

The morphology of the 0.15 AgBr-NiO is shown in Fig. 5g, revealing the integration of the AgBr NPs with the NiO surface. The images suggest a successful interfacial fusion between AgBr NPs and NiO NPs within the heterojunction. The SAED pattern



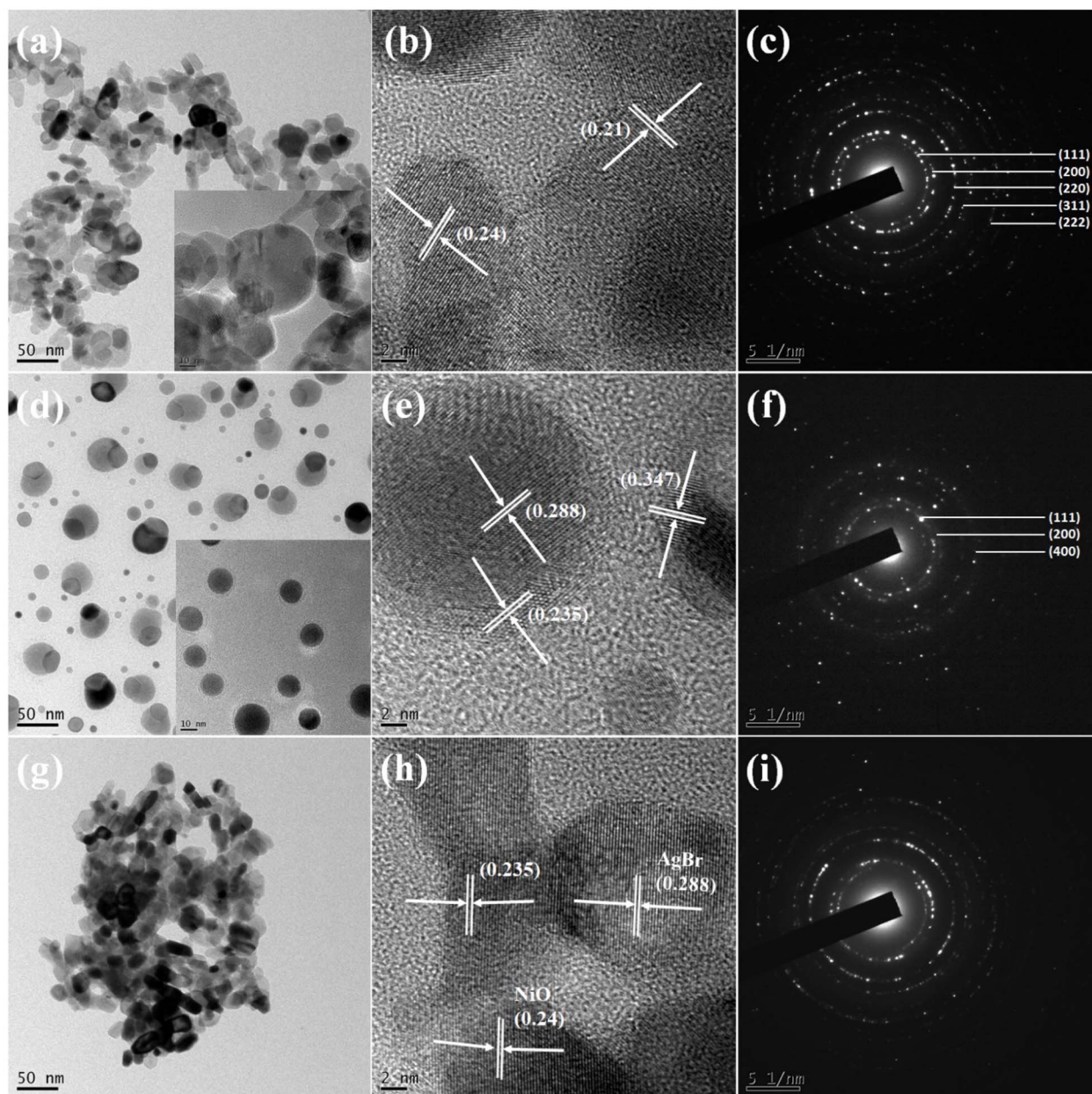


Fig. 5 TEM and HRTEM images with the selected-area electron diffraction pattern of NiO (a–c), AgBr (d–f), and 0.15 AgBr–NiO heterojunction (g–i).

confirmed the presence of both crystalline phases of pure AgBr and NiO in the heterojunction sample, as shown in Fig. 5i.

### 3.6. Optical studies

Fig. 6a displays the results of the UV-vis-DRS spectra, which were obtained to assess the optical properties of the as-synthesized photocatalyst. The absorption edges for the bare NiO and AgBr were located around 368 and 482 nm, *i.e.*, in different places. The combination of AgBr and NiO enabled effective absorption in the visible light range with a higher wavelength (426 to 534 nm), and the redshift increased regularly with the increase in the content of AgBr.

The band gap energies of pure NiO and AgBr, and the synthesized heterojunction (n-AgBr/p-NiO) were further calculated from the UV-vis-DRS spectra using the transformed Kubelka–Munk formula.<sup>21,23,26,27</sup> According to the plots of  $(\alpha h\nu)^{1/2}$  vs.  $h\nu$  (Fig. 6b), the band gaps of the singular NiO, AgBr, 0.05 AgBr–NiO, 0.1 AgBr–NiO, and 0.15 AgBr–NiO were found to be 3.4, 2.68, 2.93, 2.78, and 2.44 eV, respectively.

### 3.7. XPS analysis

The XPS spectra of the pure and heterojunction materials indicated the elemental composition, and the binding energies of the corresponding elements. In the XPS survey scan (Fig. 7a), the elements present in 0.15 AgBr–NiO, such as Ni, O, Ag, and



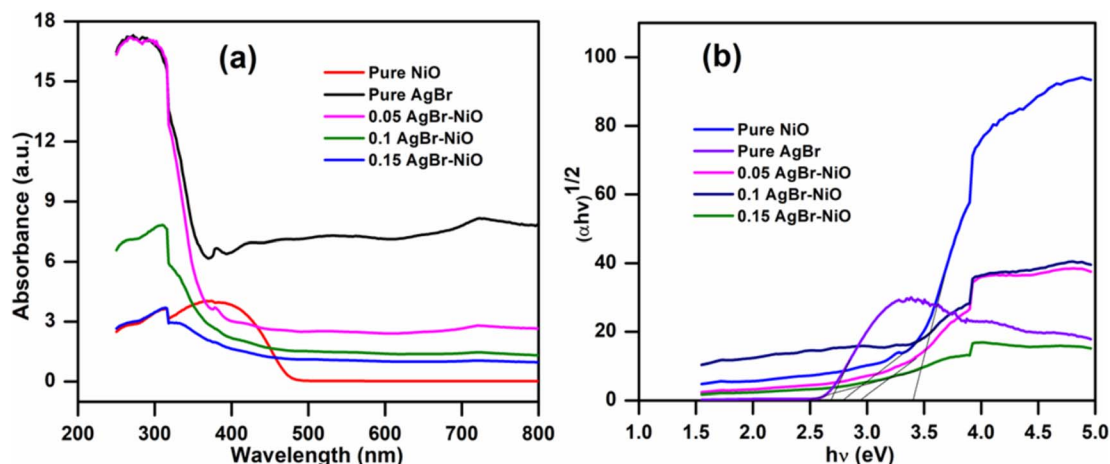


Fig. 6 (a) UV-vis-DRS of the different catalysts and (b) their corresponding Tauc plots.

Br, were found to exist at their binding energies. The deconvoluted XPS spectrum for Ni 2p (Fig. 7b) appeared at 873 and 854.1 eV for Ni 2p<sub>3/2</sub> and Ni 2p<sub>1/2</sub> with the corresponding satellite peaks at 879.6 and 861.5 eV, respectively. No additional peaks were observed for metallic Ni at 852.6 eV, indicating the existence of the NiO lattice in the binary heterojunction.<sup>48–52</sup> Fig. 7c indicates that lattice oxygen (O–Ni or Ni–O–Ni) and moisture-absorbed oxygen were present, as shown by the two high-resolution peaks at 531.3 and 529.7 eV.<sup>48,53</sup> The two doublet peaks shown in Fig. 7d obtained for Ag 3d<sub>5/2</sub> and Ag 3d<sub>3/2</sub> at 367.6 and 373.7 eV, respectively, might be possibly due to silver cations in the lattice of AgBr.<sup>54,55</sup> Furthermore, in Fig. 7e, another doublet peak emerged for Br 3p, showcasing the electronic states of Br 3p<sub>3/2</sub> and Br 3p<sub>1/2</sub> at 181.8 and 188.4 eV,

respectively.<sup>54,56</sup> The slight shift in the binding energies of the existing elements in the pristine and composite materials was evidence of the apparent electronic interaction between the p-NiO and n-AgBr materials.

### 3.8. BET measurements

As illustrated in Fig. 8, the BET surface area and porosity of the fabricated materials were ascertained *via* the nitrogen adsorption–desorption isotherms. These measurements revealed that the pure NiO had a high surface porosity and pore-size distribution compared to the pure AgBr. As shown in Fig. 8a, type IV adsorption–desorption isotherms featuring H3-hysteresis loops were obtained for each characterized material, and Table 1

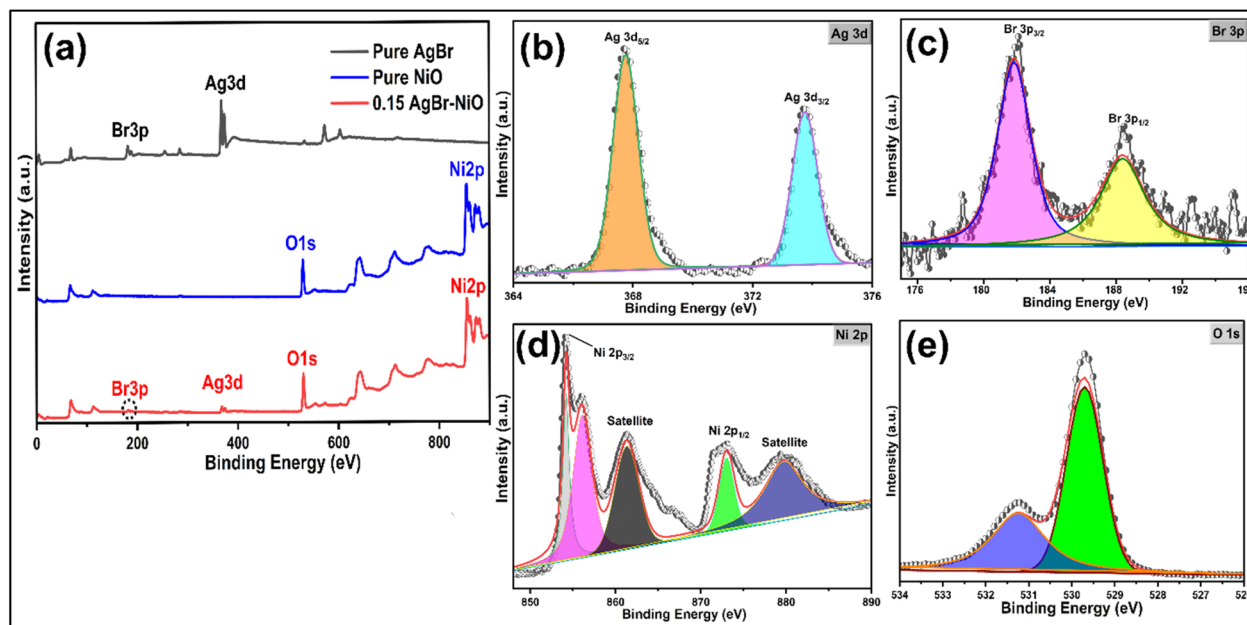


Fig. 7 XPS survey scan spectra of pure AgBr, pure NiO & 0.15 AgBr–NiO composite (a), and deconvoluted spectra of corresponding elements (b)–(e).





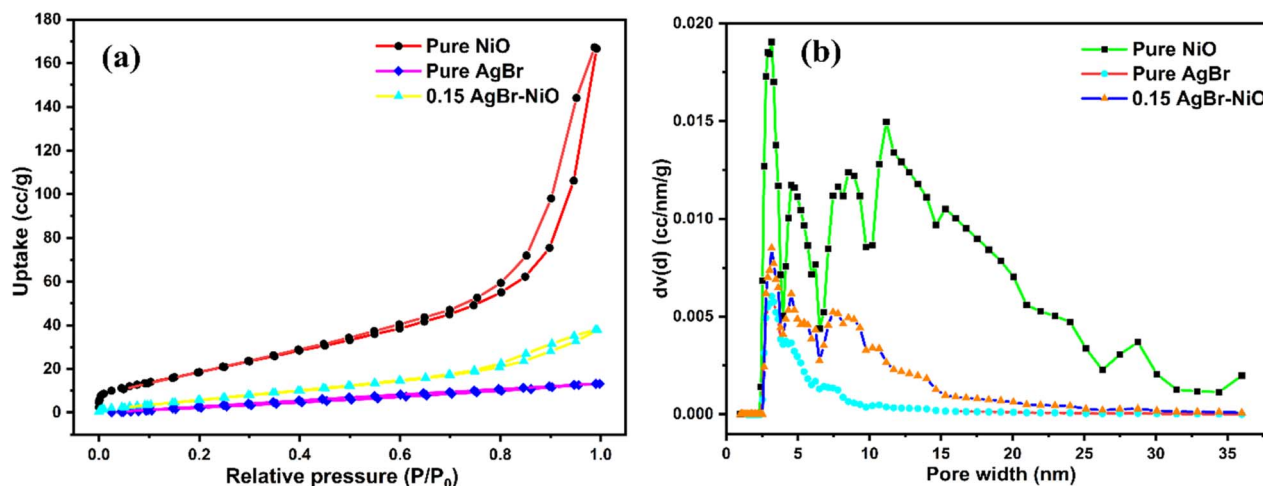


Fig. 8 (a)  $N_2$  adsorption-desorption isotherm and (b) BJH plot for the pore-size distribution.

Table 1 BET surface area and pore volume of NiO, AgBr, and 0.15 AgBr-NiO

Sample	BET-specific surface area ( $m^2 g^{-1}$ )	Pore volume ( $cm^3$ (STP) per g)
NiO	78.569	0.228
AgBr	32.142	0.019
0.15 AgBr-NiO	28.277	0.054

shows the 0.15 AgBr-NiO heterojunction was found to have a lower surface area compared to both the pristine materials, *e.g.* NiO, while retaining its mesoporosity. Also, the pore-size distribution in Fig. 8b shows that the 0.15 AgBr-NiO heterojunction material had a pores distribution in between that of the pristine NiO and pristine AgBr, whereas the pristine NiO had pores distributed up to 35 nm.

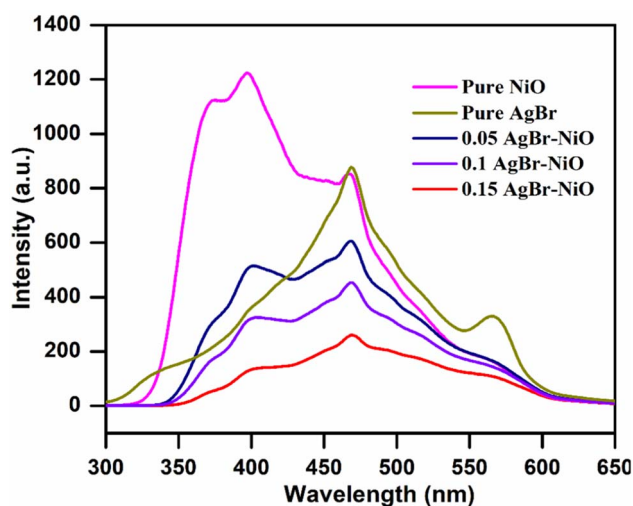


Fig. 9 PL emission spectra of pure NiO, pure AgBr, and the n-AgBr/p-NiO heterojunction in DMSO at 300 nm excitation.

### 3.9. Photoluminescence study

The photoluminescence emission of the synthesized catalyst was studied at room temperature using a 300 nm excitation wavelength to access the recombination behavior of the photogenerated ( $e^-/h^+$ ) pairs. PL measurement is crucial for understanding the efficiency of the transfer and migration of photoexcited charge carriers. The recombination of charge carriers is directly correlated with the PL emission. A stronger PL signal is generated by a rapid  $e^-$  and  $h^+$  recombination. Fig. 9 shows the comparative PL spectra of NiO, AgBr, 0.05 AgBr-NiO, 0.1 AgBr-NiO, and 0.15 AgBr-NiO under 300 nm excitation. The PL intensity of the 0.15 AgBr-NiO heterojunction was less strong than that of the other fabricated materials. It has been suggested that NiO and AgBr form a heterojunction that could enhance the photocatalytic activity by decreasing the rate of recombination of photogenerated charge carriers.

### 3.10. Photoelectrochemical measurements

Further, photoelectrochemical analyses were performed to assess the performance of the excitons ( $e^-/h^+$ ), *i.e.*, the charge-separation and transport capabilities of the synthesized materials under visible light.<sup>57</sup> We studied the charge-transfer phenomenon for the synthesized materials using electrochemical impedance spectroscopy (EIS) techniques. A Nyquist plot was obtained, as shown in Fig. S1,<sup>†</sup> consisting of a semi-circular linear pattern. The smaller diameter of the semicircle represents a lower charge-transfer resistance ( $R_{ct}$ ), corresponding to more efficient separation of charge carriers.<sup>17</sup> In Fig. S1a,<sup>†</sup> the Nyquist plot showcases the lowest charge-transfer resistance for the 0.15 AgBr-NiO composite material compared to pure NiO and pure AgBr, demonstrating the efficient photocatalytic behavior of the 0.15 AgBr-NiO composite material.

Likewise, the photocurrent responses recorded for the three semiconducting nanomaterials were similar. As shown in Fig. S1b<sup>†</sup> when switching the light on and off for 200 s, the increasing order of photocurrent density was as follows: pure NiO < pure AgBr < 0.15 AgBr-NiO. This highlights the efficient



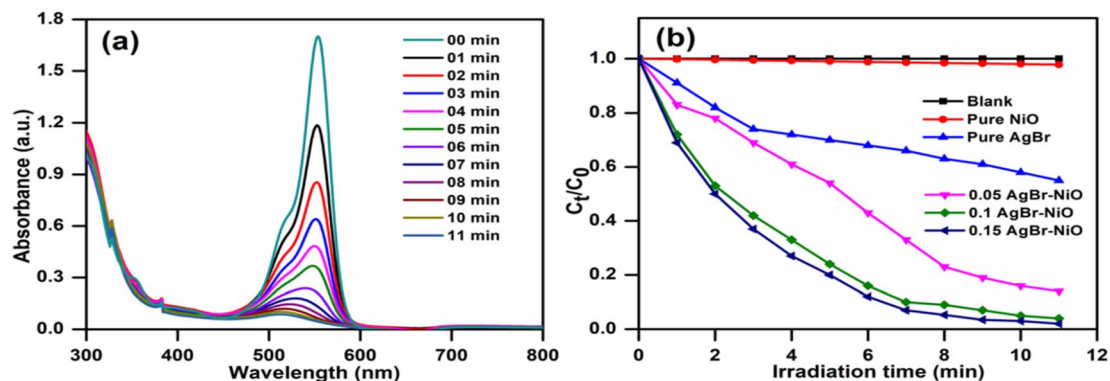


Fig. 10 (a) Changes in the absorbance of RhB over 0.15 AgBr–NiO and (b) alterations in RhB concentration as a function of time with and without various photocatalysts under visible light illumination.

charge separation, enhanced charge transport, and reduced recombination rate of the charge carriers for the composite material compared to the pure materials.

### 3.11. Photocatalytic degradation study

The photocatalytic performance of the synthesized NPs was evaluated by monitoring the degradation of model pollutants using a visible light source under atmospheric air in an aqueous suspension. To attain absorption–desorption equilibrium, the photocatalyst and pollutant solution were stirred in the dark for 30 min before illumination. Fig. 10a shows the UV-vis absorption spectra of the RhB containing photocatalyst system (0.15 NiO–AgBr) over time, demonstrating a decrease in absorbance, indicating a degradation of 97.6% in 11 min. Fig. 10b shows the change in concentration as a function of the irradiation of aqueous RhB solutions in the absence and presence of various photocatalysts. Without a catalyst, the RhB dye could not be degraded by direct photolysis, indicating it was highly stable and unable to be broken down by direct photolysis. It is important to mention that 0.15 AgBr–NiO decomposed the RhB

dye faster than the other catalysts produced. This may be due to the heterojunction between NiO and AgBr, which facilitated efficient light absorption and promoted enhanced separation of the photogenerated charge carriers.

Under analogous conditions, the photodegradation of a model colorless compound, BPA, was also investigated. Fig. 11a shows the change in absorbance at different irradiation times of an aqueous solution of BPA under analogous conditions, whereas, Fig. 11b shows the concentration change over time, both in the absence and presence of various catalysts. The results showed 85% BPA degradation in 120 min in the presence of the most active photocatalyst, *i.e.*, 0.15 AgBr–NiO.

Also, the Cr(vi) reduction was analyzed under visible light irradiation by fabricating the Cr(vi)–DPC complex and monitoring the change in absorbance at 540 nm spectrophotometrically. Fig. S2a† shows the change in the absorption spectrum with the increase in irradiation time, demonstrating a 69.6% degradation in 50 min. Further, the concentration *vs.* time plot was made, as shown in Fig. S2b,† indicating superior photocatalytic performance for the 0.15 AgBr–NiO photocatalyst compared to pure AgBr and NiO.

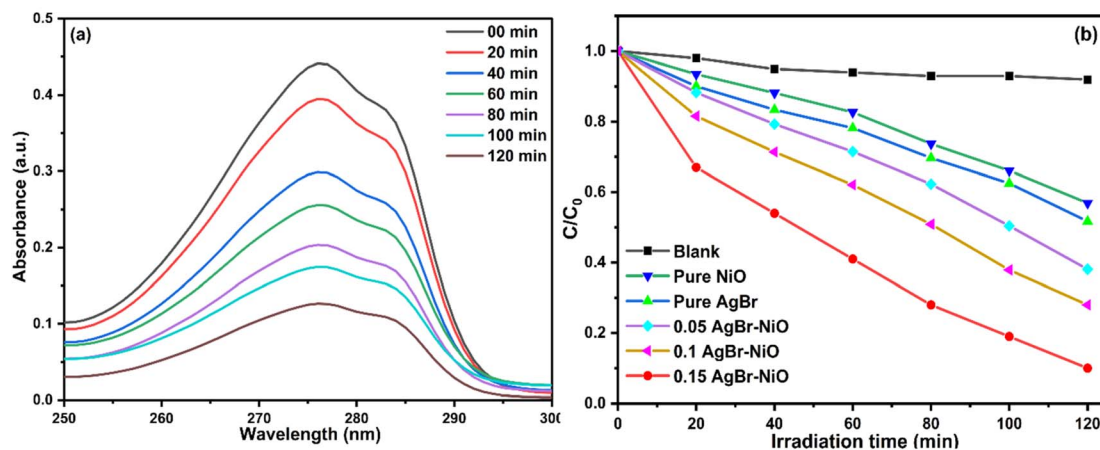


Fig. 11 (a) Changes in the absorbance of BPA over 0.15 AgBr–NiO and (b) alterations in BPA concentration as a function of time with and without various photocatalysts under visible light illumination.





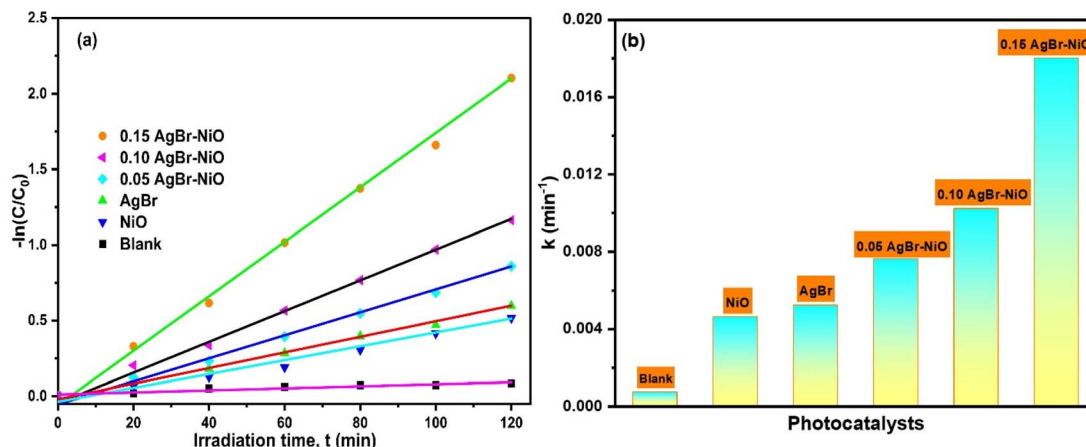


Fig. 12 (a) Pseudo first-order kinetics plot depicting  $-\ln(C/C_0)$  vs. irradiation time,  $t$  and (b) corresponding degradation rate constants of each synthesized material with the blank experiment.

Table 2 Pseudo/apparent first-order rate constants ( $k_{\text{app}}$ ) and their corresponding  $R^2$  values for each material

Sample	Apparent rate constant, $k_{\text{app}}$ ( $\text{min}^{-1}$ )	$R^2$
Blank	0.0007	0.989
Pure NiO	0.0046	0.969
Pure AgBr	0.0052	0.973
0.05 AgBr-NiO	0.0076	0.960
0.10 AgBr-NiO	0.0102	0.974
0.15 AgBr-NiO	0.0180	0.975

### 3.12. Kinetics of photodegradation

A kinetics study was performed to calculate the removal rate for the photodegradation of the model pollutants (RhB and BPA) and has been discussed using the Langmuir-Hinshelwood rate equation.<sup>58</sup> The photocatalytic reaction followed first-order kinetics, based on the following eqn (1):

$$-\ln \frac{C_0}{C_t} = kt, \quad (1)$$

where  $C_0$  and  $C_t$  are the initial and final concentrations of the pollutant at the corresponding times  $t_0$  and  $t$ , respectively, while  $k$  is the pseudo first-order rate constant. Fig. 12a shows the linear plots of  $-\ln(C/C_0)$  vs. irradiation time ( $t$ ) for the degradation of the model pollutants using different fabricated pure (AgBr and NiO) and binary composite materials (n-AgBr/p-NiO; 0.05, 0.10 and 0.15). This linear fit plot, showcasing the linear relationship between  $-\ln(C/C_0)$  and irradiation time ( $t$ ), indicates that the photocatalytic degradation of the model pollutants follows first-order reaction kinetics. Table 2 summarizes the apparent rate constant ( $k_{\text{app}}$ ) values and associated  $R^2$  values, whereas Fig. 12b shows that the highest rate of photodegradation was achieved for the 0.15 AgBr-NiO ( $0.018 \text{ min}^{-1}$ ) material, which was 3.9 times higher than that of pure NiO ( $0.0046 \text{ min}^{-1}$ ) and 3.5 times higher than pure AgBr ( $0.0052 \text{ min}^{-1}$ ). This promising degradation rate for the binary composite AgBr-NiO indicates that both components synergistically contribute to improving charge separation efficiency during photocatalysis.

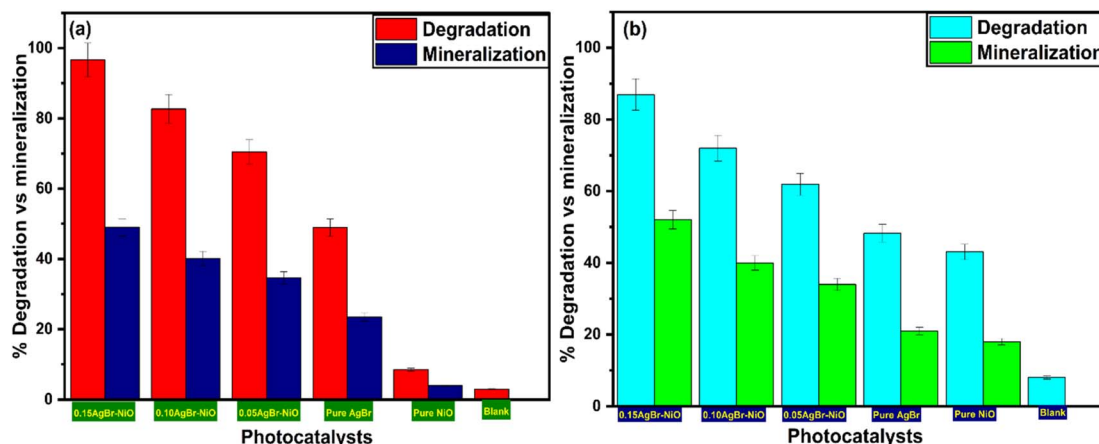


Fig. 13 Percentage degradation vs. mineralization results of RhB ((a), 11 min irradiation) and BPA ((b), 120 min irradiation) with different pure and composite materials.



### 3.13. Photomineralization study (TOC depletion)

The semiconductor-mediated photocatalyzed degradation of organic compounds is usually complex and produces various by-products, some of which may be more toxic than the parent compound. Hence, the complete mineralization of pollutants is desirable. Therefore, the photo-mineralization of both compounds was investigated by studying the decrease in total organic carbon (TOC) content over time under similar conditions.<sup>59,60</sup> The percentage mineralization of RhB and BPA with different photocatalysts and its comparison with the degradation (change in concentration) upon irradiation of an aqueous suspension under similar conditions are shown in Fig. 13a and b, respectively. The results indicated that the photocatalyst (0.15 AgBr–NiO) was the most active for the degradation and mineralization of both compounds, demonstrating its potential as the most appropriate material for environmental remediation.

### 3.14. Reusability and stability

From an application perspective, the ability to reuse a photocatalyst is influenced by its stability. Here, the recycling process was examined using recovered catalysts from an illuminated mixture of RhB under analogous conditions (0.15 AgBr–NiO) to evaluate the stability of the most active catalyst. Before using the catalyst for the next cycle, the catalyst was collected, gently rinsed with ethanol/water several times to remove unwanted components, and dried overnight at 100 °C. The photostability and recyclability test results for the 0.15 AgBr–NiO photocatalyst are shown in Fig. 14 and S3.† The XRD plot in Fig. 14a showed no significant loss in the crystalline nature of the catalyst, while the optical absorption behavior of the composite, as shown in Fig. S3,† also remained unchanged after four successive cycles (Fig. 14b), indicating the good stability of the catalyst's performance after the photoreactions. The results showed that the n–p heterojunction (0.15 AgBr–NiO) could be used repeatedly under visible light and remained stable for the removal of organic pollutants in water.

### 3.15. Adsorption isotherms

The adsorption of RhB on the surface of the photocatalyst (n–AgBr/p–NiO) was investigated using the Langmuir, Freundlich, and Temkin isotherm models. The study of adsorption isotherms is essential to understand the interaction of a photocatalyst with pollutants before photodegradation and to identify whether pollutant removal occurs through surface-mediated interactions or a direct charge-transfer process for the most efficient photocatalyst (0.15 AgBr–NiO). The linear regression eqn (2)–(4) of these models are given below.

$$\frac{C_e}{q_e} = \frac{1}{K_L q_m} + \frac{C_e}{q_m} \quad (2)$$

$$\log q_e = \log K_F + \frac{1}{n} \log C_e \quad (3)$$

$$q_e = \left( \frac{RT}{B_T} \right) \ln A_T + \left( \frac{RT}{B_T} \right) \ln C_e \quad (4)$$

here, eqn (2) represents the regression equation for the Langmuir isotherm, where the terms  $C_e$ ,  $q_e$ ,  $q_m$ , and  $K_L$  represent the concentration of RhB in the solution ( $\text{mg L}^{-1}$ ), the experimental adsorption capacity ( $\text{mg g}^{-1}$ ), the calculated adsorption capacity ( $\text{mg g}^{-1}$ ), and the Langmuir isotherm constant ( $\text{L mg}^{-1}$ ), respectively. The terms  $K_F$  and  $n$  in regression eqn (3) are the Freundlich constants. Eqn (4) is the regression equation for

Table 3 Isotherm parameters of the Langmuir, Freundlich, and Temkin adsorption models for the adsorption of RhB on 0.15 AgBr–NiO based on their linear regression equations

Isotherm models	Isotherm parameters			Error functions	
Langmuir	$q_m$	$K_L$	$R^2$	$\chi^2$	APE
	3.025	0.128	0.9958	0.431	0.45
Freundlich	$q_m$	$K_F$	$n$	$R^2$	0.0844
	2.253	0.439	0.568	0.9857	
Temkin	$A_T$	$B_T$	$R^2$	$2.59 \times 10^{-4}$	0.0111
	1.183	3661.5	0.9917		

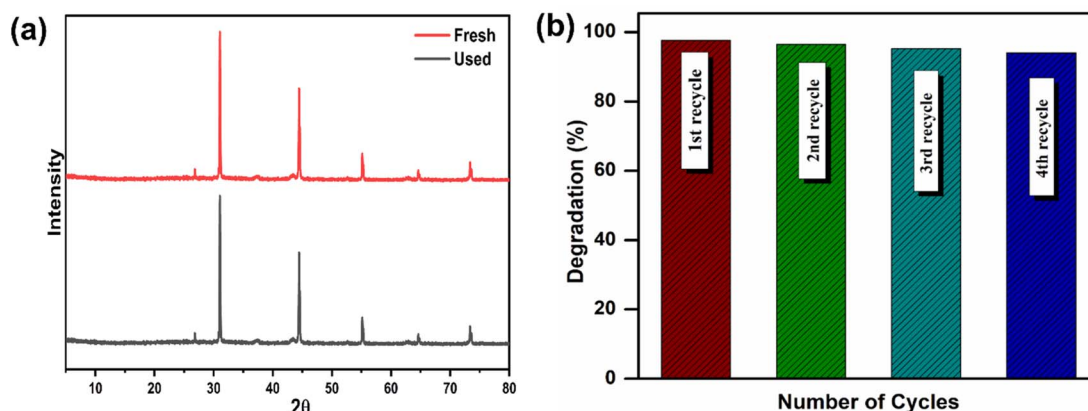


Fig. 14 Photostability (a), and recyclability (b) of the most active catalyst 0.15 AgBr–NiO for the breakdown of RhB after 4 runs under visible-light illumination.



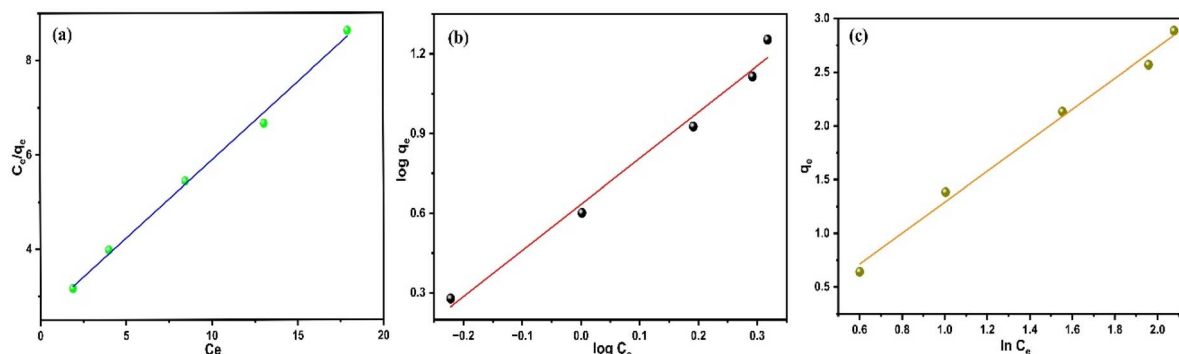


Fig. 15 Langmuir (a), Freundlich (b), and Temkin (c) isotherm model plots for the adsorption of RhB on the n-AgBr/p-NiO heterojunction.

Temkin's adsorption isotherm, where the terms  $B_T$  and  $A_T$  are constants related to this model, representing the heat of adsorption ( $\text{J mol}^{-1}$ ) and the equilibrium binding constant ( $\text{L mg}^{-1}$ ), respectively.

The adsorption data obtained using the Langmuir, Freundlich, and Temkin models are summarized in Table 3, and the corresponding linear plots for each of these models are shown in Fig. 15. The regression coefficient ( $R^2$ ) was higher for the Langmuir model than for the Freundlich and Temkin models, indicating that the order of the best-fitting model was Langmuir > Temkin > Freundlich.

In addition to these results, the dimensionless value of the separation factor ( $R_L$ ) was evaluated using eqn (5) with the values of  $C_e$  and  $K_L$ . As shown in Table S1,<sup>†</sup> the  $R_L$  value for all the concentration values was in the range of  $0 > R_L > 1$ , indicating that the adsorption was favorable. The plot of  $R_L$  versus  $C_0$  in Fig. S4<sup>†</sup> shows that the value of  $R_L$  decreased with increasing  $C_0$ .

$$R_L = \frac{1}{(1 + K_L C_0)} \quad (5)$$

It is pertinent to mention that the adsorption of pollutants on the surface of the most active catalyst (0.15 AgBr–NiO) was not significant compared to their photodegradation. This

suggested that the photogenerated charge carriers played an important role in the removal of the pollutants under our reaction conditions.

### 3.16. Antimicrobial activity

The antimicrobial activity of the synthesized catalysts was investigated against Gram-positive bacteria (*Micrococcus luteus* and *Staphylococcus aureus*) using the Agar-well diffusion method. The results in Fig. 16 revealed that 0.1 AgBr–NiO, 0.05 AgBr–NiO, and 0.15 AgBr–NiO efficiently suppressed the growth of *Staphylococcus aureus* and *Micrococcus luteus* with varying potency. It was estimated that NiO did not exhibit any growth inhibition zones against both bacterial strains, whereas AgBr did not show any growth inhibition zone against *Staphylococcus aureus*. In addition, Table 4 shows that the maximum growth inhibition zones against *Staphylococcus aureus* and *Micrococcus luteus* were demonstrated by 0.1 AgBr–NiO and 0.15 AgBr–NiO, respectively. Moreover, with the increase in the concentration of the nano-heterojunction catalysts, the growth inhibition zone increased, and no growth inhibition zone was observed against both bacterial strains at low concentrations. The reason for these findings is that the nano-heterojunction photocatalysts have a high light response, which encourages the generation of ROS that kills the cells. These findings are in agreement with

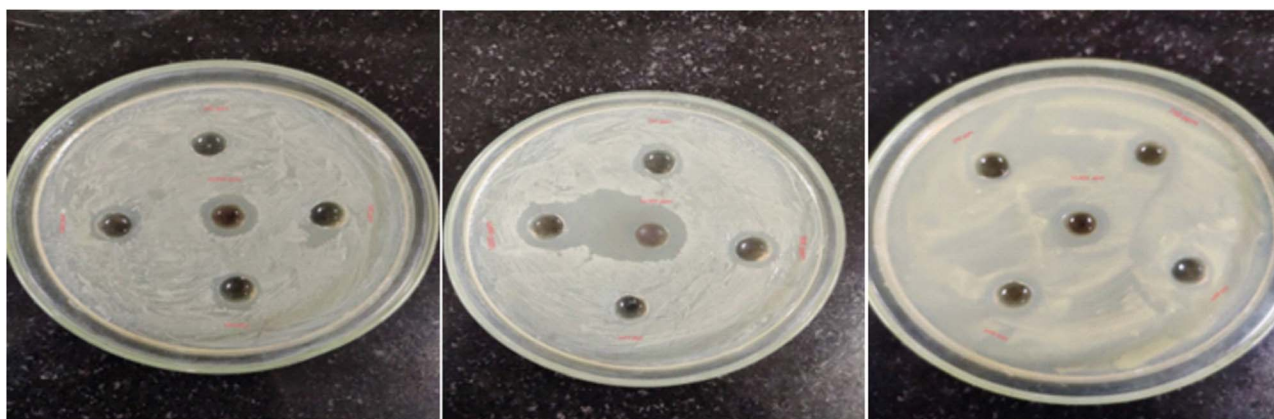


Fig. 16 Zone inhibition images of *S. aureus* (*Staphylococcus aureus*) and *M. luteus* (*Micrococcus luteus*) in the presence of all the synthesized catalysts at various concentrations ( $\mu\text{g ml}^{-1}$ ).





**Table 4** Inhibitory effect of NiO, AgBr, and n-AgBr/p-NiO heterojunctions on *S. aureus* (*Staphylococcus aureus*) and *M. luteus* (*Micrococcus luteus*)

Strain used	Concentration ( $\mu\text{g ml}^{-1}$ )	Growth inhibition zone (mm)				
		NiO	0.1 AgBr-NiO	0.05 AgBr-NiO	0.15 AgBr-NiO	AgBr
<i>S. aureus</i>	10 000	N	15	18	20	N
	1000	N	13	15	13	N
	750	N	11	N	11	N
	500	N	N	N	10	N
	250	N	N	N	N	N
<i>M. luteus</i>	10 000	N	17	17	14	15
	1000	N	12	10	12	12
	750	N	10	N	11	N
	500	N	N	N	N	N
	250	N	N	N	N	N

the photocatalytic results, revealing that the nano-heterojunction catalyst is an effective catalyst against bacteria and can remove contaminants from wastewater when illuminated with visible light.

### 3.17. Quenching experiments

Trapping studies were used to identify the primary active species involved in the photodegradation reaction. The trapping of  $\cdot\text{OH}$ ,  $\cdot\text{O}_2^-$ , and  $h^+$  during RhB photodegradation was achieved using quenchers, such as IPA, BQ, and EDTA-2Na. Fig. 17 shows the percentage degradation of RhB in the absence and presence of different scavengers containing 0.15 AgBr-NiO. It is evident from the figure that the photocatalysis of RhB was highly influenced by BQ and EDTA-2Na, indicating the prominent role of superoxides and holes during the photodegradation process. The results show that RhB's photodegradation was unaffected when isopropyl alcohol was used as an  $\cdot\text{OH}$ -radical scavenger.

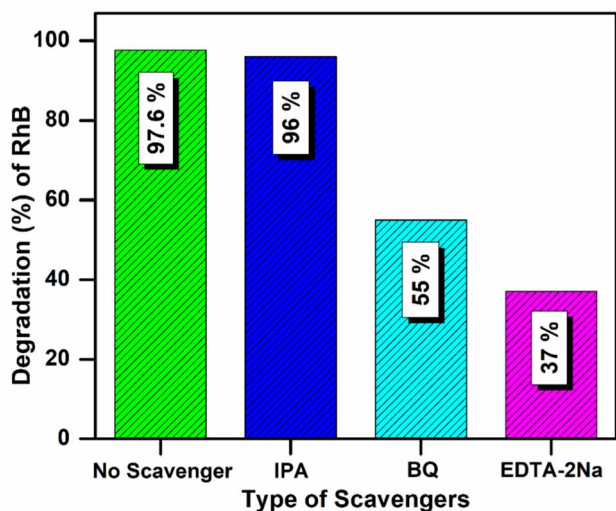


Fig. 17 Effect of various scavengers on the photocatalytic removal of model pollutants over the n-p heterojunction (0.15 AgBr/NiO) under visible-light illumination.

In addition, the photodegradation of the  $\text{Cr}(\text{vi})$ -DPC complex was also investigated using the above scavengers under similar conditions, and the results are shown in Fig. S2c.† It can be seen from the figure that BQ efficiently quenched the  $\cdot\text{O}_2^-$ , leading to a decrease in activity, while the other scavengers, such as IPA and EDTA-2Na, showed minimal effect on the photodegradation. This could be due to the fact that  $\cdot\text{O}_2^-$  were generated *via* an electron-reduction mechanism, whereby the addition of BQ could enhance the consumption of electrons in the  $\cdot\text{O}_2^-$  pathway, thereby reducing the electron availability for the reduction of  $\text{Cr}(\text{vi})$  complex. Meanwhile, IPA and EDTA-2Na significantly improved the  $\text{Cr}(\text{vi})$ -DPC reduction efficiency, with IPA preventing electron-hole pair recombination and EDTA-2Na acting as a hole-trapping agent.<sup>61,62</sup>

The involvement of hydroxyl radicals ( $\cdot\text{OH}$ ) in the photoreaction was assessed using the alkaline terephthalic acid (TA) probe method. The formation of the fluorescent product (PL signal at 425 nm), 2-hydroxy-terephthalic acid (TA-OH), resulted in the formation of  $\cdot\text{OH}$  radicals during the photodegradation process. The photocatalyst ( $\text{TiO}_2$  Degussa P25) was also used as a reference catalyst to assess the involvement of  $\cdot\text{OH}$  under comparable conditions. Fig. 18a shows a gradual increase in the PL intensity peak at 425 nm with time upon the irradiation of  $\text{TiO}_2$  under alkaline conditions, suggesting the continuous generation of hydroxyl radicals due to the formation of the fluorescence adduct TA-OH in this reaction. Fig. 18b shows the change in the PL spectra upon irradiation of the n-AgBr/p-NiO heterojunction under analogous conditions, indicating that there was no increase in the PL signal due to the insufficient generation of hydroxyl radicals under similar conditions.

In addition, the NBT phototransformation experiment was conducted to further assess the involvement of superoxide radical anions ( $\text{O}_2^{\cdot-}$ ) in the photooxidation process. Fig. 18c shows a decrease in the absorbance intensity of NBT in the presence of the n-AgBr/p-NiO photocatalyst. This corresponded to the formation of blue formazan due to the generation of  $\text{O}_2^{\cdot-}$  during visible-light irradiation, which was consistent with the quenching experiments.

Electron resonance spectroscopy (ESR) analysis was then performed to further confirm the ROS species involved during the



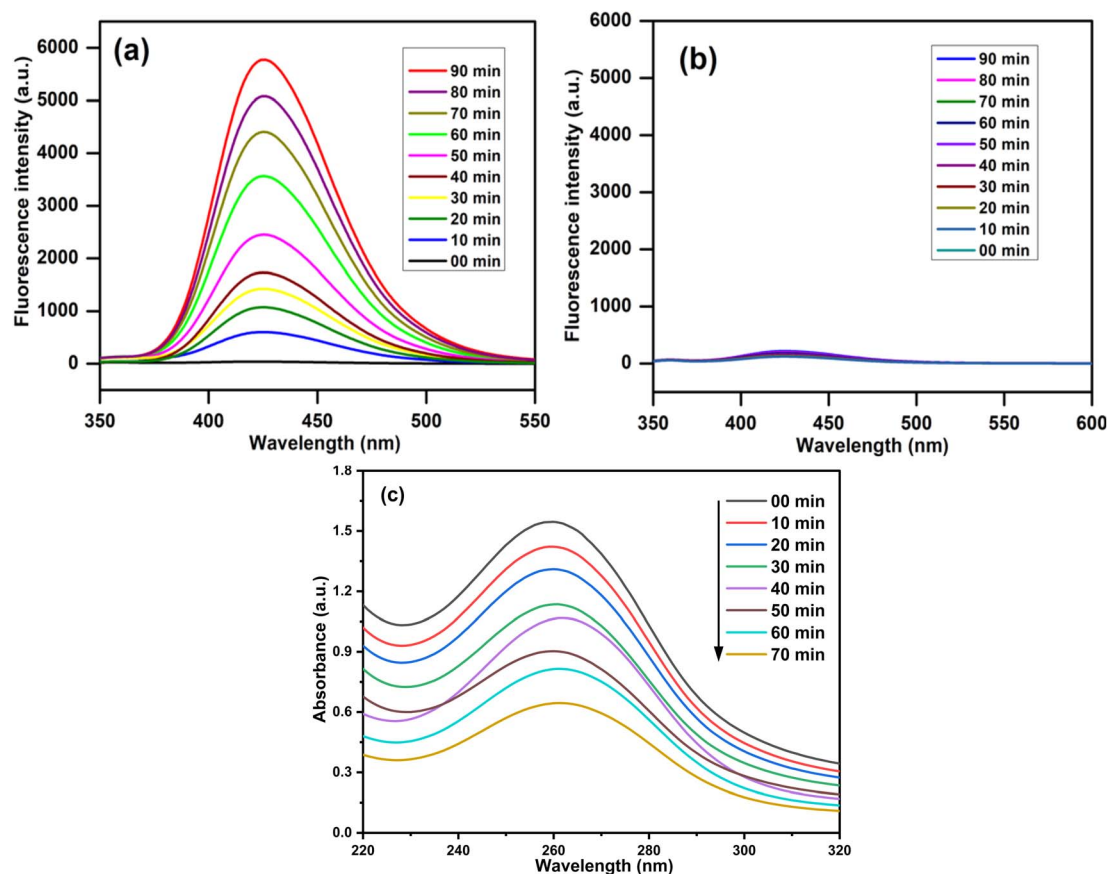


Fig. 18 Increase in PL intensity during illumination of an alkaline terephthalic acid solution ( $5 \times 10^{-4}$  M) with (a) TiO<sub>2</sub> photocatalyst, (b) 0.15 AgBr–NiO photocatalyst at an excitation of 315 nm. (c) NBT phototransformation experiment indicating a decrease in absorbance at  $\lambda_{\max}$  of 259 nm.

photodegradation reaction. The experiment was conducted using a radical trapping agent, such as 5,5-dimethyl-1-pyrroline-*N*-oxide (DMPO), which leads to the formation of radical-trapped adducts of DMPS, such as DMPO-O<sub>2</sub><sup>•−</sup> and DMPO-<sup>•</sup>OH adducts.<sup>17</sup> As shown in Fig. S5,† before irradiation (under dark conditions), a flat line was observed for the ESR signal. However, under visible-light irradiation with the methanolic suspension of the photocatalyst and air bubbling, an intense characteristic signal for the DMPO-O<sub>2</sub><sup>•−</sup> complex could be observed (Fig. S5a†). The results indicated the predominant generation of O<sub>2</sub><sup>•−</sup>, while under the aqueous suspension of the photocatalyst, a weak characteristic signal for the DMPO-<sup>•</sup>OH complex was observed, as illustrated in Fig. S5b,† indicating the lower contribution of <sup>•</sup>OH during the photocatalytic reactions. The results of this study were consistent with the results from the trapping experiments.

### 3.18. Photocatalytic mechanism

A plausible Z-scheme charge-carrier mechanism for the photocatalytic degradation of the model compounds has been proposed in Scheme 1, with the help of the band gap energy ( $E_g$ ), valence band (VB), and conduction band (CB) potentials of AgBr and NiO. The  $E_g$  values for AgBr and NiO have already been derived from the Tauc plots depicted in Fig. 6b. The VB and CB values of each were calculated using the following eqn (6)–(8):<sup>5</sup>

$$E_{CB} = X - E_e - \frac{1}{2}E_g \quad (6)$$

$$E_{VB} = E_{CB} + E_g, \quad (7)$$

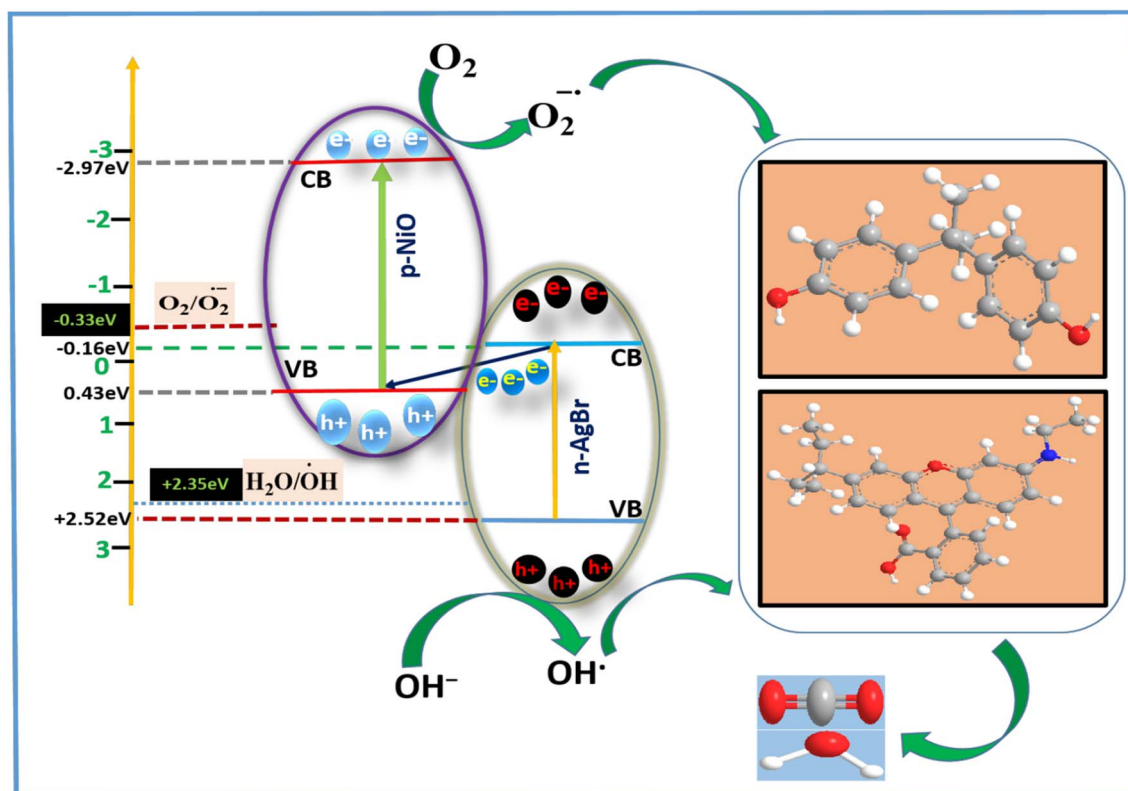
where  $E_{CB}$  and  $E_{VB}$  correspond to the CB and VB potentials of semiconducting nanomaterials,  $X$  is the absolute electronegativity, and  $E_e$  is the free electron energy of the material on the H-scale (4.50 eV).

$$X = [\chi(A)^a \chi(B)^b \chi(C)^c]^{1/(a+b+c)} \quad (8)$$

here,  $\chi$  denotes the absolute electronegativity of each element, and  $a$ ,  $b$ ,  $c$  represent the number of corresponding elements available in each semiconducting material.

Additionally, the band edge potentials of AgBr and NiO were deduced by Mott–Schottky (MS) plots, also shown in Fig. S6.† The Fermi level band potentials ( $E_{fb}$ ) obtained for each material helped to calculate the values of  $E_{CB}$  and  $E_{VB}$  for each photocatalyst (AgBr and NiO). The resulting MS plot with a positive slope represented an n-type semiconductor, while an MS plot with a negative slope represented a p-type semiconductor. In the case of AgBr, the positive MS slope obtained showed its n-type semiconducting behavior, while the negative slope of the MS plot for NiO showed its p-type semiconducting behavior.





**Scheme 1** Schematic representation of the Z-scheme electron-transfer pathway in the NiO–AgBr heterojunction for the photodegradation of RhB and BPA.

The experimental  $E_g$  values for AgBr and NiO were 2.68 eV and 3.4 eV, respectively, obtained from the Tauc plots. The calculated CB position of AgBr was  $-0.16$  eV, which was not much more negative than the standard redox potential of oxygen  $E_0(\text{O}_2/\text{O}_2^{\bullet-})$ , i.e.  $-0.33$  V vs. NHE. Therefore, it may not produce superoxide radicals ( $\text{O}_2^{\bullet-}$ ). The CB position of NiO was  $-2.97$  eV, which was a much more negative value than the required potential for  $\text{O}_2^{\bullet-}$  generation. The calculated VB positions for AgBr and NiO were 2.52 eV and 0.43 eV, respectively. Meanwhile, AgBr possessed a higher positive value than the standard redox potential of hydroxide  $E_0(\text{OH}^-/\text{OH}^\bullet)$ , i.e.,  $+2.35$  eV vs. NHE. Therefore, under visible light irradiation, the photoinduced excitation of electron from the VB of AgBr to the CB of AgBr cannot produce superoxide radicals. Instead, the excited  $e^-$  gets transported to the VB of NiO, where subsequent excitation to CB of NiO establishes a Z-scheme  $e^-$  transfer mechanism. In this process, the  $\text{O}_2^{\bullet-}$  generated near the CB of NiO and the  $\text{OH}^\bullet$  at the VB of AgBr effectively interacted with the model compounds, facilitating their degradation.

## 4. Conclusion

In summary, the n-AgBr/p-NiO heterojunction photocatalyst has been successfully synthesized using a facile deposition-precipitation approach and applied for the degradation of RhB and BPA. The results of the photodegradation and

mineralization studies demonstrated that the nano-heterojunction photocatalyst (AgBr–NiO) was more active than the pure samples (AgBr and NiO). The superoxide radical acted as the main reactive species in the photocatalytic reaction, as evidenced by the trapping experiments study. The heterojunction formed between AgBr and NiO could promote the spatial separation of ( $e^-$ – $h^+$ ) pairs, resulting in greatly improved photodegradation activity. Furthermore, *in vitro* antibacterial studies were conducted, which revealed that AgBr–NiO exhibited high antimicrobial activity against *Staphylococcus aureus* and *Micrococcus luteus*. Specifically, the AgBr–NiO photocatalyst showed microbial inhibition zones of 20 mm and 17 mm, respectively, compared to the pure samples and standard drug. The proposed method demonstrates good potential for removing contaminants from water systems and treating pathogenic bacterial strains using photodynamic therapy, as shown clearly and effectively in the current study.

## Data availability

Data are available upon reasonable request.

## Author contributions

Murad Z. A. Warshagha: conceptualization, formal analysis, methodology, writing – original draft, writing – review and





editing. Ziyaur Rasool: conceptualization, visualization, formal analysis, methodology, software, writing – review and editing. Mohammad Saud Athar: methodology, formal analysis, writing – review and editing. Mohammad Muneer: resources, supervision, visualization, project administration, funding acquisition, writing – review and editing. Hatem M. Altass: methodology, data curation. Raad Felemban: methodology, software. Abdelrahman S. Khder: software, data curation. Saleh A. Ahmed: methodology, investigation, funding acquisition, visualization, writing – review and editing.

## Conflicts of interest

The authors declare that they have no competing financial interests or personal relationships that could have appeared to influence the work reported in this study.

## Acknowledgements

The authors extend their appreciation to Umm Al-Qura University, Saudi Arabia, for funding this research through grant number: 25UQU4320545GSSR03. This research work was funded by Umm Al-Qura University, Saudi Arabia under grant number: 25UQU4320545GSSR03.

## References

- 1 M. S. Athar, A. Khan, I. Ahmad and M. Muneer, *New J. Chem.*, 2024, **48**, 5346–5361.
- 2 Z. Shi, Z. Chen, Y. Zhang, X. Wang, T. Lu, Q. Wang, Z. Zhan and P. Zhang, *Sep. Purif. Technol.*, 2022, **288**, 120717.
- 3 C. Nefzi, B. Askri, B. Yahmadi, N. El Guesmi, J. M. García, N. Kamoun-Turki and S. A. Ahmed, *J. Photochem. Photobiol., A*, 2022, **431**, 114041.
- 4 Y. Chen, S. Pu, D. Wang, Y. Zhang, G. Wan, Q. Zhao and Y. Sun, *J. Solid State Chem.*, 2023, **321**, 123857.
- 5 Z. Rasool, M. S. Athar and M. Muneer, *Environ. Sci. Pollut. Res.*, 2024, **31**, 31259–31272.
- 6 M. P. Rayaroth, D. Oh, C. S. Lee and Y. S. Chang, *Chemosphere*, 2022, **294**, 133788.
- 7 M. S. Athar, Z. Rasool, M. Muneer, H. M. Altass, I. I. Althagafi and S. A. Ahmed, *ACS Omega*, 2023, **8**, 38272–38287.
- 8 I. Ahmad, M. S. Athar, M. Muneer, H. M. Altass, R. F. Felemban and S. A. Ahmed, *Surf. Interfaces*, 2024, **45**, 103819.
- 9 Y. Bai, L. Ye, L. Wang, X. Shi, P. Wang, W. Bai and P. K. Wong, *Appl. Catal., B*, 2016, **194**, 98–104.
- 10 Y. Ao, L. Xu, P. Wang, C. Wang, J. Hou, J. Qian and Y. Li, *Appl. Surf. Sci.*, 2015, **355**, 411–418.
- 11 C. G. Anchiet, E. C. Severo, C. Rigo, M. A. Mazutti, R. C. Kuhn, E. I. Muller, E. M. M. Flores, R. F. P. M. Moreira and E. L. Foletto, *Mater. Chem. Phys.*, 2015, **160**, 141–147.
- 12 H. Gao, Y. Zhang, H. Xia, X. Mao, X. Zhu, S. Miao, M. Shi and S. Zha, *Dalton Trans.*, 2022, **51**, 11876–11883.
- 13 H. Gao, Y. Han, Y. Wang, H. Xia, X. Zhu, D. Wang, Y. Zhang, X. Mao and L. Zhang, *Sep. Purif. Technol.*, 2024, **346**, 127548.
- 14 M. Mokhtar Mohamed, G. Osman and K. S. Khairou, *J. Environ. Chem. Eng.*, 2015, **3**, 1847–1859.
- 15 M. Danish, M. Saud Athar, I. Ahmad, M. Z. A. Warshagha, Z. Rasool and M. Muneer, *Appl. Surf. Sci.*, 2022, **604**, 154604.
- 16 C. Castañeda, D. Santos, J. S. Hernández, A. Álvarez, H. Rojas, R. Gómez, F. Rajabi, J. J. Martínez and R. Luque, *Chemosphere*, 2023, **315**, 137606.
- 17 M. S. Athar and M. Muneer, *J. Alloys Compd.*, 2024, **980**, 173385.
- 18 Z. Xu, J. Zhong, M. Li and H. Yang, *Mater. Lett.*, 2022, **323**, 132544.
- 19 Y. Ran and J. Zhong, *Mater. Lett.*, 2022, **328**, 133133.
- 20 M. Z. A. Warshagha, M. Muneer, I. I. Althagafi and S. A. Ahmed, *RSC Adv.*, 2023, **13**, 5013–5026.
- 21 M. Z. A. Warshagha and M. Muneer, *Surf. Interfaces*, 2021, **26**, 101394.
- 22 M. Danish, Z. Rasool, H. Iqbal, R. Fatima, S. Kumar and M. Muneer, *Mater. Adv.*, 2023, **4**, 3506–3520.
- 23 M. Z. A. Warshagha and M. Muneer, *Langmuir*, 2020, **36**, 9719–9727.
- 24 X. Hu, G. Wang, J. Wang, Z. Hu and Y. Su, *Appl. Surf. Sci.*, 2020, **511**, 145499.
- 25 M. S. Athar and M. Muneer, *Photochem. Photobiol. Sci.*, 2023, **22**, 695–712.
- 26 M. Z. A. Warshagha and M. Muneer, *Int. J. Environ. Anal. Chem.*, 2022, **102**, 6339–6358.
- 27 M. Z. A. Warshagha and M. Muneer, *Environ. Nanotechnol., Monit. Manage.*, 2022, **18**, 100728.
- 28 M. S. Athar, M. Danish and M. Muneer, *J. Environ. Chem. Eng.*, 2021, **9**, 105754.
- 29 M. S. Athar, N. Saleem, I. Ahmad, M. Fazil, T. Ahmad and M. Muneer, *Mater. Today Sustain.*, 2024, **26**, 100779.
- 30 D. Chatterjee and S. Dasgupta, *J. Photochem. Photobiol., C*, 2005, **6**, 186–205.
- 31 H. Gao, Y. Zhang, H. Xia, X. Zhu, X. Mao, W. Zhao, S. Miao and M. Shi, *Colloids Surf., A*, 2023, **663**, 131030.
- 32 M. Z. A. Warshagha and M. Muneer, *ACS Omega*, 2022, **7**, 30171–30183.
- 33 S. Feizpoor and A. Habibi-Yangjeh, *Mater. Res. Bull.*, 2018, **99**, 93–102.
- 34 K. Arora, M. Kaur, H. Singh, S. Karthikeyan and T. S. Kang, *Appl. Surf. Sci.*, 2021, **553**, 149555.
- 35 Y. Xie, H. Zhang, J. Lv, J. Zhao, D. Jiang and Q. Zhan, *Appl. Surf. Sci.*, 2022, **578**, 152074.
- 36 A. Saadati, A. Habibi-Yangjeh, S. Feizpoor, R. Keyikoglu and A. Khataee, *J. Photochem. Photobiol., A*, 2022, **431**, 114034.
- 37 L. Yosefi and M. Haghighi, *Appl. Catal., B*, 2018, **220**, 367–378.
- 38 C. V. Khedkar, A. S. Vedpathak, A. V. Dhotre, K. D. Daware, Y. D. Kolekar, S. D. Sartale, S. W. Gosavi and S. I. Patil, *Chem. Phys. Impact.*, 2023, **6**, 100153.
- 39 Y. Ku, C. N. Lin and W. M. Hou, *J. Mol. Catal. A: Chem.*, 2011, **349**, 20–27.
- 40 R. K. Gupta, K. Ghosh and P. K. Kahol, *Phys. E: Low-Dimens. Syst. Nanostructures*, 2009, **41**, 617–620.
- 41 Z. Khan, M. Khannam, N. Vinothkumar, M. De and M. Qureshi, *J. Mater. Chem.*, 2012, **22**, 12090–12095.



- 42 H. Y. Chen, L. G. Qiu, J. D. Xiao, S. Ye, X. Jiang and Y. P. Yuan, *RSC Adv.*, 2014, **4**, 22491–22496.
- 43 P. Laokul, N. Kanjana, R. Ratchatane, S. Ruangjan, N. Kotsarn, A. Chingsungnoen and P. Poolcharuansin, *Mater. Chem. Phys.*, 2023, **295**, 127112.
- 44 Q. Hu, W. Li, D. I. Abouelamaiem, C. Xu, H. Jiang, W. Han and G. He, *RSC Adv.*, 2019, **9**, 20963–20967.
- 45 W. Wu, X. Lv, J. Wang and J. Xie, *J. Colloid Interface Sci.*, 2017, **496**, 434–445.
- 46 P. E. Saranya and S. Selladurai, *New J. Chem.*, 2019, **43**, 7441–7456.
- 47 Z. T. Khodair, N. M. Ibrahim, T. J. Kadhim and A. M. Mohammad, *Chem. Phys. Lett.*, 2022, **797**, 139564.
- 48 W. Mohammed, M. Matalkeh, R. M. Al Soubaihi, A. Elzatahry and K. M. Saoud, *ACS Omega*, 2023, **8**, 40063–40077.
- 49 W. Huang, S. Ding, Y. Chen, W. Hao, X. Lai, J. Peng, J. Tu, Y. Cao and X. Li, *Sci. Rep.*, 2017, **7**, 1–11.
- 50 A. Kotta and H. K. Seo, *Appl. Sci.*, 2020, **10**, 5415.
- 51 C. Wu, S. Deng, H. Wang, Y. Sun, J. Liu and H. Yan, *ACS Appl. Mater. Interfaces*, 2014, **6**, 1106–1112.
- 52 X. Geng, D. Lahem, C. Zhang, C. J. Li, M. G. Olivier and M. Debliquy, *Ceram. Int.*, 2019, **45**, 4253–4261.
- 53 S. Kumaravel, B. Avula, C. Chandrasatheesh, T. Niyitanga, R. Saranya, I. Hasan, T. Abisheik, R. S. Rai, V. Pandiyan and K. Balu, *Spectrochim. Acta, Part A*, 2024, **310**, 123972.
- 54 F. Puga, J. A. Navío and M. C. Hidalgo, *Photochem. Photobiol. Sci.*, 2023, **22**, 549–566.
- 55 H. Yin, M. Zhang, J. Yao, Y. Luo, P. Li, X. Liu and S. Chen, *Mater. Sci. Semicond. Process.*, 2020, **105**, 104688.
- 56 W. Chen, M. Wilmet, T. G. Truong, N. Dumait, S. Cordier, Y. Matsui, T. Hara, T. Takei, N. Saito, T. K. N. Nguyen, T. Ohsawa, N. Ohashi, T. Uchikoshi and F. Grasset, *Heliyon*, 2018, **4**, e00654.
- 57 M. Danish, M. Qamar, M. Suliman and M. Muneer, *Adv. Compos. Hybrid Mater.*, 2020, **3**, 570–582.
- 58 H. D. Tran, D. Q. Nguyen, P. T. Do and U. N. P. Tran, *RSC Adv.*, 2023, **13**, 16915–16925.
- 59 M. J. Batista-Barwinski, N. Butzke-Souza, R. Radetski-Silva, F. Tiegs, R. Laçoli, G. A. Venturieri, P. R. M. Miller, J. O. Branco, R. Ariento-Neto and C. M. Radetski, *J. Environ. Sci. Health, Part B*, 2024, **59**, 131–141.
- 60 M. Sun, Y. Xie, J. Huang, C. Liu, Y. Dong, S. Li and C. Zeng, *J. Environ. Manage.*, 2024, **363**, 121393.
- 61 Q. Wang, S. Zheng, W. Ma, J. Qian, L. Huang, H. Deng, Q. Zhou, S. Zheng, S. Li, H. Du, Q. Li, D. Hao and G. Yang, *Appl. Catal., B*, 2024, **344**, 123669.
- 62 B. Ning, Z. Chen, Y. Cai, F. X. Xiao, P. Xu, G. Xiao, Y. He, L. Zhan and J. Zhang, *Langmuir*, 2024, **40**, 9144–9154.

